Chemical Science

ROYAL SOCIETY OF CHEMISTRY

EDGE ARTICLE

View Article Online
View Journal

Cite this: DOI: 10.1039/d6sc01887d

All publication charges for this article have been paid for by the Royal Society of Chemistry

Synchronizing O_2 adsorption and proton-coupled electron transfer in carboxylated quinoline-linked covalent organic frameworks to boost photocatalytic H_2O_2 production

Hao Wang,[a] Junjiang Zong,[a] Shiyuan Wei,[a] Meng Li,[a] Xiaodong Sun,[c] Liqun Ye,[d] Jianhan Huang,*[a] Jiawei Li,*[a] You-Nian Liu[a] and Tianyi Ma[b]

Covalent organic frameworks (COFs) have great potential for photocatalytic H_2O_2 production, but they are frequently limited by the incompatibility between the thermodynamic O_2 adsorption and the kinetic proton-coupled electron transfer (PCET). The precise design and facile construction of a coordinated microenvironment that integrates "strong O_2 adsorption-rapid PCET" in a single COF remains a great challenge. Herein, for the first time, we developed a *de novo* construction strategy and successfully synthesized a carboxylated quinoline-linked QL-TTB-COF. The quinoline rings reshape the local electronic structure at the active dipyridyl N sites, significantly strengthening Yeager-type side adsorption of O_2 and sharply boosting H_2O_2 production *via* one-step $2e^-$ oxygen reduction reaction. Meanwhile, the introduced –COOH not only improves the hydrophilicity of the pore channels but also serves as the proton reservoir, accelerating the overall reaction kinetics by establishing proton transfer networks. In particular, the dipyridyl and –COOH trigger the $4e^-$ water oxidation reaction, offering additional O_2 and protons for H_2O_2 production. Benefiting from the synergistic "strong O_2 adsorption-rapid PCET" mechanism, QL-TTB-COF achieves a remarkable H_2O_2 yield rate of 7848 μmol g^{-1} h^{-1}, and it ranks among the highest levels of the COF-based photocatalysts. This work highlights the significance of precisely controlling the thermodynamic O_2 adsorption and the kinetic proton transfer at the molecular level of the COF-based photocatalysts for H_2O_2 production.

Received 6th March 2026
Accepted 12th May 2026

DOI: 10.1039/d6sc01887d

rsc.li/chemical-science

Introduction

Utilizing solar energy to drive oxygen (O_2) reduction for hydrogen peroxide (H_2O_2) production represents a sustainable artificial photosynthesis strategy.[1] Essentially, it stores light energy in chemical bonds *via* the $O_2 + 2H^+ + 2e^- \rightarrow H_2O_2$ reaction ($2e^-$ ORR).[2] The overall efficiency of $2e^-$ ORR typically depends on the synergistic supply capability of three reactant species: gas-phase O_2, photo-generated electrons (e^-), and protons (H^+).[3,4] However, the current photocatalytic efficiency of H_2O_2 production remains severely constrained due to the dynamic mismatch in the concerted supply of these species at the active sites. Therefore, it is imperative to establish a specific catalytic microenvironment, which can thermodynamically enable the precise capture and activation of O_2, and kinetically ensure the rapid and synchronous transfer of e^- and H^+.

Covalent organic frameworks (COFs) have emerged as an ideal platform for photocatalytic H_2O_2 production, owing to their customizable backbone, permanent porosity, and exceptional stability.[5,6] The local electronic structure of the COFs can be facilely modulated to promote rapid transfer of photo-generated electrons. However, the interfacial transfer of photo-generated electrons typically occurs at femtosecond to picosecond timescale, while the diffusion-controlled proton transfer lags significantly behind, and this spatiotemporal mismatch often results in kinetically limited proton-coupled electron transfer (PCET).[7,8] It is found that introducing specific functional groups, such as –COOH, –OH and $–SO_3H$, to the COFs is effective.[9,10] They can act as proton relays by forming hydrogen-bond networks, effectively reducing the activation energy of proton diffusion and enabling the protons to be promptly transferred to the active sites.[11,12] Nevertheless, the overall reaction rate is still largely restricted by the consistent

[a]College of Chemistry and Chemical Engineering, Key Laboratory of Micro and Nano Material Interface Science, Central South University, Changsha, 410083, China. E-mail: jianhanhuang@csu.edu.cn; lijiawei@csu.edu.cn

[b]Centre for Atomaterials and Nanomanufacturing (CAN), RMIT University, Melbourne, VIC 3000, Australia. E-mail: tianyi.ma@rmit.edu.au

[c]Institute of Clean Energy Chemistry, Key Laboratory for Green Synthesis and Preparative Chemistry of Advanced Materials, College of Chemistry, Liaoning University, Shenyang, 110036, China

[d]College of Materials and Chemical Engineering, Key Laboratory of Inorganic Nonmetallic Crystalline and Energy Conversion Materials, China Three Gorges University, Yichang 443002, China

compatibility between the thermodynamic O_2 adsorption and the rate-determining PCET step,[13,14] which stems from the much lower diffusion of H^+ ($\sim 2.39 \times 10^{-9}$ m^2 s^{-1}, 300 K) than that of O_2 ($\sim 1.88 \times 10^{-5}$ m^2 s^{-1}).[11,15] Furthermore, the inherent hydrophobicity of the COFs backbone creates a substantial proton transfer barrier, thereby forming a "proton-deficient" microenvironment around the active sites.[7,16] In this context, precisely designing and carefully constructing a coordinated microenvironment that integrates "strong O_2 adsorption-rapid PCET" in a single COF remains a great challenge.

For this purpose, for the first time, an ingenious dual regulation strategy targeting both strong O_2 adsorption and rapid transfer of e^- and H^+ was proposed for the COF photocatalysts. To the best of our knowledge, despite extensive research on PCET alone,[7–10,17–20] studies on O_2 adsorption synergistic PCET remain largely unexplored.[8] Through a facile one-pot solvothermal method, three COFs (TTB-COF, BQ-TTB-COF and QL-TTB-COF, Fig. 1a) were comparatively synthesized. It is found that transformation of the imine bonds to quinoline rings not only improves the conjugation degree and chemical stability of the COFs, but also effectively modulates the local electronic structure, promoting Yeager-type side adsorption of O_2 at the dipyridyl N sites and facilitating O_2 reduction for H_2O_2 production *via* one-step $2e^-$ ORR pathway. Meanwhile, the embedded side-chain –COOH in QL-TTB-COF not only enhances the hydrophilicity of the pore channels, but also provides ample H^+ for the $2e^-$ ORR, thereby accelerating the overall reaction kinetics by rapid PCET. Moreover, this precise

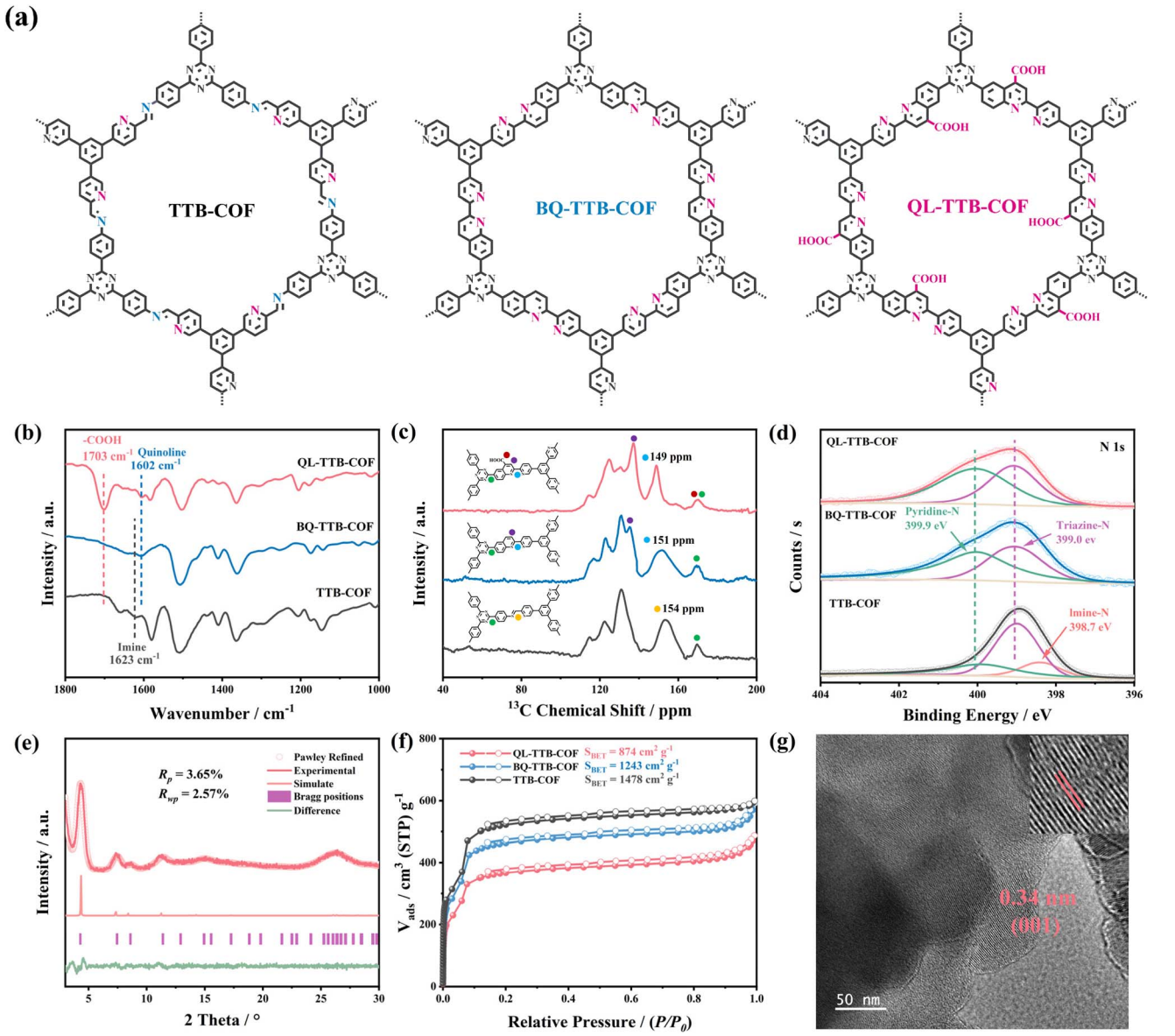

Fig. 1 (a) Chemical structure of TTB-COF, BQ-TTB-COF and QL-TTB-COF, (b) FT-IR spectra, (c) solid-state ^{13}C NMR spectra, (d) N 1s spectra of TTB-COF, BQ-TTB-COF and QL-TTB-COF, (e) PXRD pattern of QL-TTB-COF, (f) N_2 adsorption–desorption isotherms of TTB-COF, BQ-TTB-COF and QL-TTB-COF, (g) TEM image of QL-TTB-COF.

regulation ignites the $4e^-$ water oxidation reaction (WOR), which offers additional O_2 and H^+ for the $2e^-$ ORR. Benefiting from the promotion of O_2 adsorption and the optimization of continuous PCET process, QL-TTB-COF achieves a H_2O_2 yield rate up to 7848 μmol g^{-1} h^{-1} in pure water, significantly higher than BQ-TTB-COF (3523 μmol g^{-1} h^{-1}) and TTB-COF (1444 μmol g^{-1} h^{-1}), and ranks among the highest levels of the COF-based photocatalysts.

Results and discussion

Synthesis and characterization of the photocatalysts

The triazine ring is a N-rich and electron-deficient moiety, which is beneficial for light absorption, and it is proven the promising photocatalytic unit.[21] Additionally, the pyridine N of 5,5′,5″-(1,3,5-benzenetriyl)tris[2-pyridinecarboxaldehyde] (BTPA) can serve as the active sites for O_2 adsorption.[22] Therefore, TTB-COF was firstly synthesized by a typical Schiff base reaction using 4,4′,4″-(1,3,5-triazine-2,4,6-triyl)trianiline (TAPT) and BTPA as the monomers, the formed imine bonds and the adjacent pyridine N may be the active sites for O_2 adsorption and subsequent ORR. Afterwards, by a one-pot three-component reaction, the novel quinoline-linked BQ-TTB-COF was constructed using TAPT and BTPA as the monomers and triethylamine as the vinyl source.[23] It is observed that the imine bonds are transformed to the quinoline rings with the dipyridyl structure. It can be expected that the formed unique dipyridyl N can significantly enhance O_2 adsorption, sharply boosting H_2O_2 production *via* one-step $2e^-$ ORR. Furthermore, by a three-component Doebner reaction, we introduced side-chain –COOH in BQ-TTB-COF and fabricated the carboxylated quinoline-linked QL-TTB-COF.[24] The induced –COOH is anticipated to form hydrogen-bond transfer networks and provide abundant H^+ for H_2O_2 production by accelerating the overall reaction kinetics.

The chemical structure of the three COFs was firstly characterized by Fourier transform infrared (FT-IR) spectroscopy. Compared to the imine-linked TTB-COF, the attenuation of C=N stretching at approximately 1623 cm^{-1} and the appearance of quinoline rings at around 1602 cm^{-1} verify the quinoline-linked BQ-TTB-COF and QL-TTB-COF (Fig. 1b and S1).[23] Additionally, the peak at 1703 cm^{-1} can be assigned to –COOH in QL-TTB-COF.[24] The solid-state ^{13}C NMR spectra of TTB-COF exhibit the characteristic imine C at 154 ppm (Fig. 1c), while this signal is absent for BQ-TTB-COF and QL-TTB-COF, where those of quinoline rings present at approximately 151 ppm. The characteristic –COOH peak of QL-TTB-COF presents at 168 ppm, overlapping with the triazine peak.[24,25] X-ray photoelectron spectroscopy (XPS) supported the above conclusions. Fig. 1d demonstrates that the imine bonds at 398.7 eV are completely vanished for BQ-TTB-COF and QL-TTB-COF, while a strong pyridine N signal of quinoline rings appears at 399.9 eV, and the conversion of imine bonds to quinoline rings is successful.[25] Additionally, in C 1s spectra of QL-TTB-COF, the characteristic peak at 289.1 eV can be assigned to the side-chain –COOH (Fig. S2–S4).[24,25]

The crystallinity of the photocatalysts was evaluated by powder X-ray diffraction (PXRD). They exhibit similar diffraction patterns and display intense reflections in the low-angle region at 4.1° (Fig. 1e, S5 and S6).[26,27] The simulation results indicate that the experimental PXRD data of these COFs closely match the simulated AA stacking model, with Pawley fitting analysis yielding *R* factors of less than 5% for both unweighted-profile (R_p) and weighted-profile (R_{wp}). Based on N_2 adsorption–desorption isotherms (Fig. 1f), the Brunauer–Emmett–Teller (BET) surface area of TTB-COF, BQ-TTB-COF, and QL-TTB-COF is calculated to be 1478 m^2 g^{-1}, 1243 m^2 g^{-1}, and 874 m^2 g^{-1}, with average pore size of about 2.3 nm, 2.2 nm, and 2.0 nm, respectively (Fig. S7). The microstructure of the COFs was characterized using scanning electron microscopy (SEM) and transmission electron microscopy (TEM). The SEM images in Fig. S8 reveal that they are irregular nanoparticles. The HR-TEM images in Fig. 1g show that crystalline domains with ordered lattice fringes with an interplanar *d*-spacing of 0.34 nm, coherent with the QL-TTB-COF interlayer spacing of the simulated pattern (Fig. S9–S11).

Photocatalytic H_2O_2 production

The photocatalytic H_2O_2 production performance of the three COFs was comparatively investigated in pure water without any sacrificial agent under visible-light irradiation (300 W Xe lamp, $\lambda \geq 420$ nm) at room temperature. The H_2O_2 amount was determined using potassium iodide colorimetric analysis and the standard curve in Fig. S12. As shown in Fig. 2a, QL-TTB-COF exhibits almost constant H_2O_2 production during one-hour operation, with the yield rate of 7848 μmol g^{-1} h^{-1}, significantly higher than BQ-TTB-COF (3523 μmol g^{-1} h^{-1}) and TTB-COF (1444 μmol g^{-1} h^{-1}). This enhanced photocatalytic activity is likely attributed to the synergistic integration of the introduced dipyridyl structure and –COOH, which thermodynamically facilitates O_2 adsorption and kinetically accelerates proton transfer, thereby accelerating the rate-determining PCET process. Certainly, this yield rate ranks among the highest levels of the materials in similar applications (Fig. 2b and Table S1). To evaluate the light utilization efficiency of QL-TTB-COF in pure water, its apparent quantum yield (AQY) under monochromatic light irradiation at 420 nm is measured to be 8.8% (Fig. S13). Additionally, its solar-to-chemical conversion efficiency (SCC) reaches 0.16%, outperforming that of naturally occurring plants (~0.10%).[28] The optimal dosage of QL-TTB-COF is 0.125 mg mL^{-1} (Fig. S14), and it has high compatibility with various aqueous matrices, including Xiangjiang River water in China, seawater, and tap water (Fig. S15).

The generation and decomposition of H_2O_2 are two competing pathways for H_2O_2 production, and the photocatalytic decomposition experiments of H_2O_2 (100 μM L^{-1}) indicate that QL-TTB-COF displays negligible degradation of H_2O_2. After one hour of visible light irradiation, the H_2O_2 concentration remains above 95% of its initial value (Fig. S16), illustrating its continuous generation over its decomposition. Noticeably, by evaluating the generation rate constant (K_f) and the decomposition rate constant (K_d), Fig. 2c displays that QL-

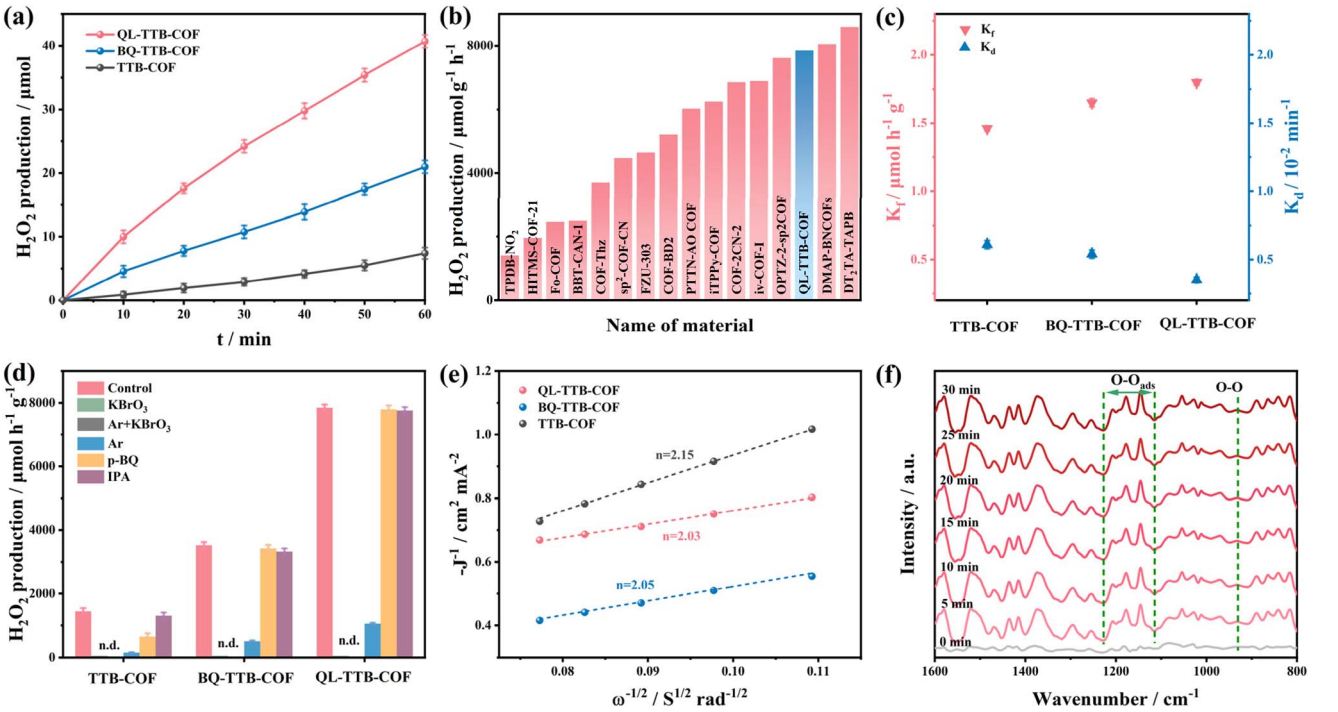

Fig. 2 (a) Time-dependent H_2O_2 production of the photocatalysts (5 mg catalyst in 40 mL water, $\lambda > 420$ nm Xe lamp), (b) H_2O_2 production rate of QL-TTB-COF in comparison with other COF-based photocatalysts, (c) K_f and K_d of H_2O_2, (d) control experiments, (e) Koutecky–Levich plots by RDE measurements at −1.0 V (*vs.* Ag/AgCl), (f) *In situ* DRIFTS spectra QL-TTB-COF.

TTB-COF has the highest K_f while the lowest K_d among the three photocatalysts, indicating that the introduction of –COOH groups does not promote H_2O_2 adsorption and decomposition. QL-TTB-COF was reused for five cycles without significant deactivation (Fig. S17), with its pore structure and chemical composition well preserved (Fig. S18), demonstrating the robust durability required for sustained H_2O_2 production.[5]

Reaction pathway for H_2O_2 production

A series of control experiments were performed to investigate the reaction pathways for H_2O_2 production. As shown in Fig. 2d, the addition of $KBrO_3$ (e^- scavenger) results in nearly undetectable H_2O_2 for the COFs. In contrast, the incorporation of isopropanol (IPA, $^{\bullet}OH$ scavenger) has negligible effect. This indicates that the primary source of H_2O_2 originates from the $2e^-$ ORR, rather than the $2e^-$ WOR.[18] Interestingly, the addition of *p*-benzoquinone (*p*-BQ, $^{\bullet}O_2^-$ scavenger) sharply reduces H_2O_2 production for TTB-COF, while those of BQ-TTB-COF and QL-TTB-COF remain largely unaffected, even at high concentrations of *p*-BQ (0.01–0.1 mM, Fig. S19). That is to say, for TTB-COF, $^{\bullet}O_2^-$ plays a pivotal role as the key intermediate for H_2O_2 production, and H_2O_2 is produced according to both one-step $2e^-$ ORR and two-step $2e^-$ ORR.[29] This phenomenon may arise from the readily occurring O_2 detachment as the imine N and the pyridine N simultaneously engage in Yeager-type side adsorption. In contrast, the H_2O_2 production on BQ-TTB-COF and QL-TTB-COF does not involve the $^{\bullet}O_2^-$ species. That is, after the imine bonds were converted to the quinoline rings with dipyridyl structure, the O_2 adsorption is greatly enhanced by Yeager-type, thereby generating H_2O_2 *via* the one-step $2e^-$ ORR. Notably, it is seen that H_2O_2 can be detected in Ar-saturated solution, whereas no H_2O_2 is observed in Ar-saturated $KBrO_3$ solution, manifesting that the photogenerated holes participate in the H_2O oxidation process *via* $4e^-$ WOR, and the produced O_2 and H^+ may facilitate the $2e^-$ ORR for H_2O_2 production.[8,18]

The isotope labeling experiments were thereafter conducted using $^{18}O_2$ and $H_2{}^{16}O$ to distinguish the oxygen source for H_2O_2. MnO_2 was added to degrade the produced H_2O_2 to O_2, and the released O_2 was analyzed by gas chromatography-mass spectrometry (GC-MS).[30] The results in Fig. S20 mean that both of $^{18}O_2$ and $^{16}O_2$ are present in the system, meaning that the generated H_2O_2 is originated from both $2e^-$ ORR and $4e^-$ WOR.[18] After combining these two peaks, $^{18}O_2$ and $^{16}O_2$ account for 92.8% and 7.2% of the total H_2O_2. That is, the dissolved atmospheric O_2 for $2e^-$ ORR and *in situ* generated O_2 based on $4e^-$ WOR account for 92.8% and 7.2%. Surprisingly, we observe that the contribution of the $4e^-$ WOR for H_2O_2 production on QL-TTB-COF is much greater than that on BQ-TTB-COF (3.5%) and TTB-COF (1.1%, Table S2). It can be concluded that the introduced –COOH in QL-TTB-COF trigger the efficiency of $4e^-$ WOR, offering additional O_2 and H^+ for the ORR. Meanwhile, the O_2 evolution in the catalytic system was detected under saturated Ar-saturated $KBrO_3$ solution (Fig. S21), and it is evident that the O_2 evolution capacity of QL-TTB-COF is greatly higher than BQ-TTB-COF and TTB-COF. Furthermore, the analysis of charge density difference is in favor of this conclusion. As compared with the H_2O molecules on TTB-COF and BQ-

TTB-COF, QL-TTB-COF can lose more electrons (Fig. S22), suggesting that it has a stronger ability to oxidize H_2O and produce O_2.

By the electrochemical analysis on a rotating disk electrode (RDE), the selectivity to the $2e^-$ ORR was further evaluated. The results in Fig. 2e indicate that the electron transfer number for BQ-TTB-COF and QL-TTB-COF is closer to 2 (Fig. S23–S25), which is conducive to the $2e^-$ ORR pathway.[2] The reactive oxygen species in the ORR were further investigated by EPR experiment using 5,5-dimethyl-1-pyrroline-oxide (DMPO) as the spin trapping agent. As shown in Fig. S26, TTB-COF exhibits the characteristic six-line peak of DMPO-$^{\bullet}O_2^-$, whereas BQ-TTB-COF and QL-TTB-COF do not display this peak, confirming that the formation of dipyridyl structure significantly restrains the generation of $^{\bullet}O_2^-$. Furthermore, the amount of $^{\bullet}O_2^-$ in the system was quantitatively determined by nitro blue tetrazolium salt (NBT), a reagent that is specifically captured only by $^{\bullet}O_2^-$. As shown in Fig. S27, negligible $^{\bullet}O_2^-$ is detected for BQ-TTB-COF and QL-TTB-COF, further clarifying that H_2O_2 production on BQ-TTB-COF and QL-TTB-COF occurs *via* one-step $2e^-$ ORR rather than two-step $2e^-$ ORR.[22,31] Noticeably, no characteristic signals of $^{\bullet}OH$ radicals were detected for the three COFs, ruling out the $2e^-$ WOR (Fig. S28). *In situ* diffuse reflect infrared Fourier transform (DRIFTS) spectroscopy was carried out and it reveals that QL-TTB-COF has a strong signal in the range of 1115–1295 cm^{-1}, which can be assigned to the –O–O– vibration (Fig. 2f).[31] Within 10 min of irradiation, the intensity of this signal remains unchanged and retains thereafter. Additionally, a new vibration at 910 cm^{-1} is observed for QL-TTB-COF, which should be ascribed to the 1,4-peroxy intermediate, thereby confirming the Yeager-type side adsorption of O_2.[22,31]

Photoelectrochemical properties and electronic structure

Ultraviolet-visible diffuse reflectance spectroscopy of the three COFs in Fig. 3a reveals a progressive red shift from TTB-COF to BQ-TTB-COF and to QL-TTB-COF, and the introduced quinoline rings and –COOH should be the main reasons due to the extended conjugation.[32] The optical band gaps of TTB-COF, BQ-TTB-COF, and QL-TTB-COF were determined to be 2.76 eV, 2.48 eV and 2.32 eV, respectively (Fig. S29). In addition, the positions of conduction band (CB) and valence band (VB) of the COFs were determined by Mott–Schottky (M–S) electrochemical measurements combined with optical band gap, and their CB and VB potentials were determined (Fig. S30–S35) as follows: TTB-COF at −1.01 V and +1.75 V, BQ-TTB-COF at −0.90 V and +1.58 V, and QL-TTB-COF at −0.85 V and +1.47 V (*vs.* NHE). These values indicate the thermodynamic feasibility of the one-step $2e^-$ ORR (+0.68 V *vs.* NHE) and the $4e^-$ WOR (+1.23 V *vs.* NHE) for H_2O_2 production (Fig. 3b). In particular, the geometric optimization of the COFs was performed, and the highest occupied molecular orbital (HOMO)-lowest unoccupied molecular orbital (LUMO) energy was calculated (Fig. S36). Noticeably, the energy level diagram exhibits similar trends with the measured CB and VB, particularly, it reflects the narrowest band gap of QL-TTB-COF among the three photocatalysts.[18]

The charge dynamics of the COFs were then investigated and the EIS Nyquist plot reveals that QL-TTB-COF owns the lowest charge transfer resistance (R_{ct}), implying its highest charge

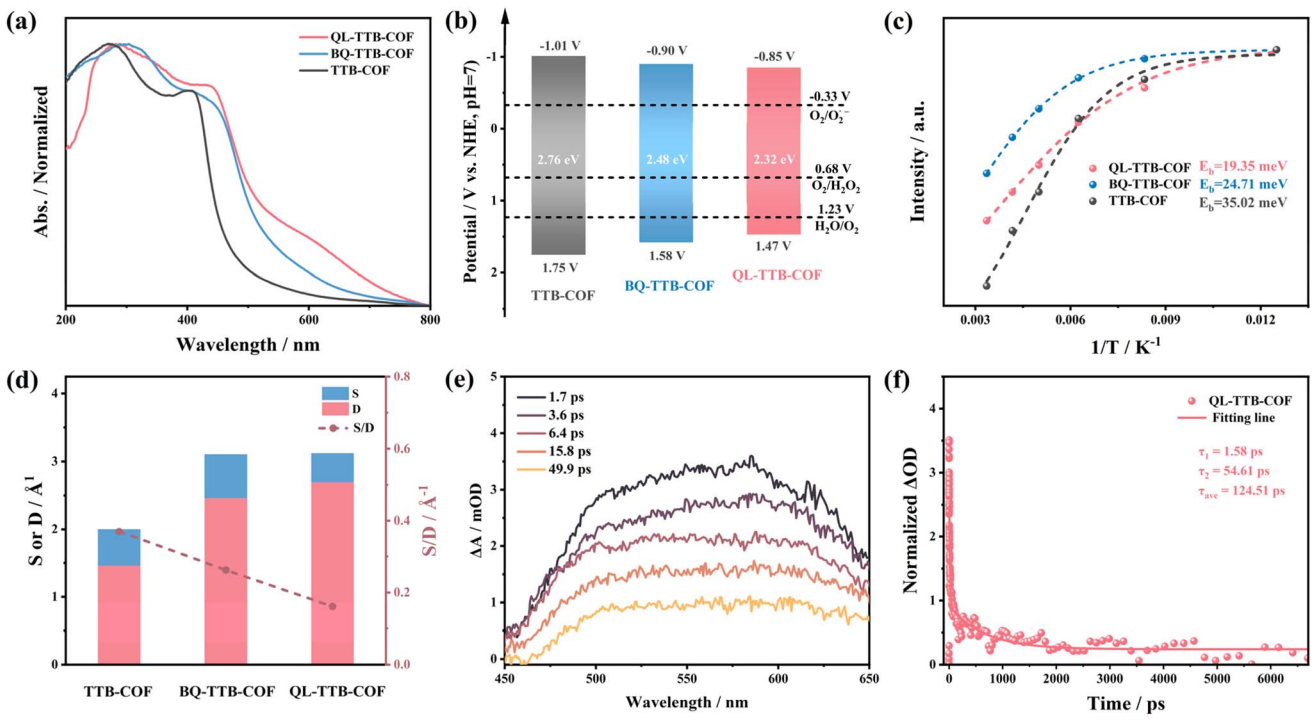

Fig. 3 (a) Ultraviolet-visible diffuse reflectance spectra, (b) band structure, (c) temperature-dependent photoluminescence spectra, (d) electron–hole distribution, (e) Fs-TAS spectra at different decay time, (f) decay kinetic curves of QL-TTB-COF.

transfer efficiency and greatest mobility capability of photo-generated carriers (Fig. S37 and Table S3).[33] Moreover, under visible light irradiation, QL-TTB-COF has rapid photo-current response, confirming its greatest transfer efficiency of photo-generated carriers (Fig. S38). Additionally, under visible light irradiation and at the same frequency, QL-TTB-COF has the much lower slope in the Mott–Schottky plot, implying its higher carrier concentration (Fig. S39). Meanwhile, the photoluminescence (PL) and time-resolved PL (TRPL) spectroscopy of the COFs were studied and it can be seen that under 342 nm excitation, QL-TTB-COF has much reduced PL emission intensity, manifesting that it can effectively inhibit the recombination of photo-generated electrons and holes (Fig. S40).[6,34] According to the TRPL results (Fig. S41), the average lifetime of QL-TTB-COF is 3.19 ns, slightly longer than BQ-TTB-COF (2.97 ns) and much longer than TTB-COF (1.35 ns). The temperature-dependent PL (TD-PL) spectroscopy was thereafter analyzed and the exciton binding energy (E_b) was determined. As can be observed in Fig. 3c and Fig. S42, the E_b values of TTB-COF, BQ-TTB-COF, and QL-TTB-COF were 35.02 meV, 24.71 meV and 19.35 meV, respectively. The minimum E_b of QL-TTB-COF implies the highest exciton dissociation efficiency. That is, the conversion of the imine bonds to quinoline rings as well as the introduction of the –COOH on the COFs effectively modulates the local electronic structure. The electron–hole distribution at excited state was investigated by time-dependent DFT calculations. As shown in Fig. 3d and Table S4, the S/D value of QL-TTB-COF is significantly lower than BQ-TTB-COF and TTB-COF, suggesting the rapid separation and transfer of photo-generated carriers.[35] The femtosecond time–resolved absorption (fs–TA) spectroscopy was then conducted (Fig. 3e, f and S43), and it is observed that these COFs exhibit positive photo-induced absorption (PIA) bands in 450–650 nm, with the absorption peak around 590 nm. This is attributable to photo-induced electron absorption and persists for duration exceeding microseconds.[23] Particularly, QL-TTB-COF has the strongest ESA absorption, confirming its most effective carrier separation capability. The kinetic fitting results reveal a dual-exponential decay process, characterized by a short lifetime (τ_1) and a long lifetime (τ_2), corresponding to electron trapping and electron transfer kinetics, respectively. According to the kinetic curve, it is seen that QL-TTB-COF has a much longer average lifetime ($\tau_{avg} = 124.51$ ps) compared to BQ-TTB-COF ($\tau_{avg} = 62.85$ ps) and TTB-COF ($\tau_{avg} = 21.97$ ps), indicating the highest exciton dissociation and charge transfer efficiency.[15]

O_2 adsorption and proton transfer efficiency

To investigate the different effects of the imine N and dipyridyl N on O_2 adsorption, the O_2 adsorption on the three COFs were evaluated *via* temperature-programmed O_2 desorption (O_2-TPD) (Fig. 4a). Compared to TTB-COF (119 °C), BQ-TTB-COF and QL-TTB-COF have broad and intense high-temperature desorption peaks (130 °C and 133 °C, respectively). Quantitative analysis demonstrates that the O_2 adsorption capacity of QL-TTB-COF is up to 0.0319 mmol g^{-1}, much higher than BQ-TTB-COF (0.0282 mmol g^{-1}) and TTB-COF (0.0081 mmol g^{-1}). That is, the newly formed dipyridyl structure in BQ-TTB-COF effectively enhances O_2 adsorption, and the induced –COOH in QL-TTB-COF further strengthens the O_2 adsorption by induction effect. Moreover, the electrostatic potential (ESP) simulations localize these electrons near imine N, pyridine N, and quinoline N,[36,37] and the quantitative surface analysis in Fig. 4b demonstrates that, compared with TTB-COF and BQ-TTB-COF, the electrostatic potential of QL-TTB-COF extends towards a more negative region. The introduction of lone pair electrons leads to a more negative electrostatic potential energy.[38] Therefore, in QL-TTB-COF, the introduced dipyridyl and –COOH facilitate the binding of O_2 at the active dipyridyl N sites.

Meanwhile, it is clear that the introduced dipyridyl and –COOH improves the hydrophilicity of the COFs due to the much less water contact angle (Fig. 4c). The improved wettability enables rapid water penetration, ensuring the smooth proton transfer at the solid–liquid interface, which is a critical prerequisite for the subsequent PCET process.[11,17] In addition, Fig. 4d displays that TTB-COF, BQ-TTB-COF, and QL-TTB-COF exhibit distinct water vapor adsorption inflection points under relative pressure (P/P_0), with the values at 0.62, 0.50 and 0.40, respectively. The low inflection point pressure of QL-TTB-COF indicates easy H_2O cluster formation and smooth passage of H_2O molecules in the pore channels *via* capillary effects.[39] Consequently, the introduction of –COOH promotes H_2O molecules transfer in the pore channels, thereby enhancing proton transfer and O_2 utilization. In addition, strong capillary forces within the hydrophilic channels drive the rapid movement of water molecules, quickly transferring the generated H_2O_2 into the bulk solution, thereby effectively preventing the secondary decomposition of H_2O_2 at the reaction sites. Significantly, the possible mechanism of hydrogen-bond formation between the hydrogen atom of H_2O and the oxygen atom of –COOH as H_2O adsorption on QL-TTB-COF was systematically investigated using an independent gradient model based on Hirshfeld distribution analysis combined with scatter plot visualization (Fig. 4e and S44).[40] Furthermore, the real-space functional analysis characterized interaction strengths using key bond points derived from molecular atomic theory. It is noticeable that H_2O molecules adsorbed on QL-TTB-COF exhibit more negative $\lambda_2(\rho)$ and higher δ_g at bond critical points compared to BQ-TTB-COF and TTB-COF.[41] This unique electronic structure implies much stronger interaction between –COOH and H_2O in QL-TTB-COF.

To investigate the effect of –COOH on the proton conduction, the AC impedance spectroscopy was conducted at the temperature range of 303–353 K and 90% relative humidity (Fig. S45). It can be seen that the proton conductivity rate of QL-TTB-COF (6.48×10^{-2} S cm^{-1}) is much greater than BQ-TTB-COF (1.16×10^{-4} S cm^{-1}) and TTB-COF (8.59×10^{-4} S cm^{-1}).[17] That is, introducing –COOH on the COFs really accelerates the proton conduction. In addition, the proton transfer activation energies (E_a) of the three COFs were calculated using the temperature-dependent Arrhenius equation, yielding 0.25 eV, 0.34 eV and 0.36 eV, respectively (Fig. 4f).[11] Of course, these E_a are all lower than 0.4 eV, indicating that the proton conduction follows the Grotthuss mechanism, where the H^+ are transferred in the hydrogen-bond networks.[42] Obviously,

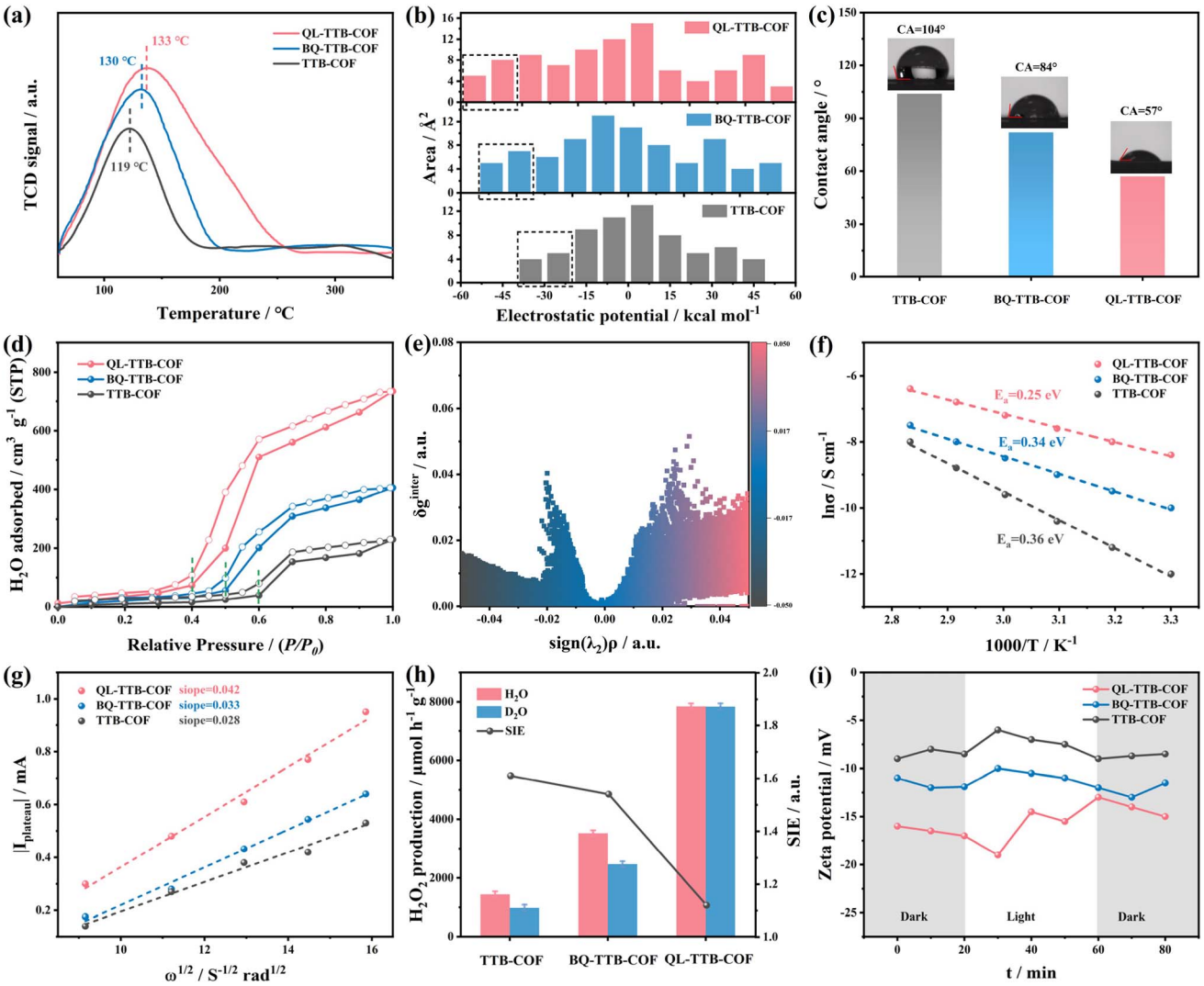

Fig. 4 (a) O_2-TPD curves, (b) quantitative electrostatic potential profiles, (c) water contact angles, (d) water vapour desorption isotherms, (e) adsorption of H_2O and the corresponding independent gradient model based on Hirshfeld scatter plots, (f) Arrhenius plots from the proton conductivity *versus* temperature, (g) $I_{plateau}$ *vs.* $\omega^{1/2}$ linear fitting based on Levich equation, (h) isotope experiments in D_2O and H_2O, (i) zeta potential as the function of the time.

QL-TTB-COF owns the highest proton conductivity rate and the lowest E_a among the three COFs, and dense hydrogen-bond networks are readily formed in the pore channels, thereby accelerating the proton conduction in the frameworks. Moreover, the rotating disk electrode curves of the COFs were analyzed. Compared to BQ-TTB-COF and TTB-COF, QL-TTB-COF has the higher plateau current with all rotational speeds (Fig. S23–S25), implying the increased proton density and the promoted proton transfer. This conclusion is further experimentally verified by the proton diffusion coefficient (Dobs, H^+), and Fig. 4g shows that the H^+ in QL-TTB-COF is evidently greater than that in BQ-TTB-COF and TTB-COF.[43] It is noteworthy that the Dobs and H^+ values discussed here reflect the overall influence of the photocatalysts on proton transfer at the electrode interface, rather than the absolute diffusion coefficient of H^+ in the solution.

Furthermore, the photocatalytic H_2O_2 experiments were comparatively conducted in H_2O and D_2O. Fig. 4h displays that compared to H_2O, the activity of BQ-TTB-COF and TTB-COF in D_2O decreases by 21% and 24%, respectively, while QL-TTB-COF remains almost unchanged. That is, the –COOH in QL-TTB-COF enhance the proton utilization. In addition, the solvent isotope effect (SIE), expressed as k_H/k_D, was determined for these photocatalysts.[18] Interestingly, the SIE values of BQ-TTB-COF and TTB-COF are within the range of 1.2 to 4, suggesting that the proton transfer is indeed the rate-determining step (RDS). In contrast, the SIE value of QL-TTB-COF is close to 1, indicating that the RDS does not involve the proton transfer. In conclusion, the introduced dipyridyl in BQ-TTB-COF optimizes the thermodynamic O_2 adsorption, while the overall reaction rate is severely limited by the kinetically restricted proton transfer. Nevertheless, the hydrophilic pore channels in

QL-TTB-COF by introducing –COOH overcomes the mass transfer barrier, making the proton transfer no longer the RDS. Moreover, the –COOH can ionize to release H^+, and these H^+ can be quickly transferred to the active sites for the ORR at the initial stage. That is, the introduction of the –COOH on QL-TTB-COF achieves a perfect match between O_2 adsorption and PCET process, ensuring highly efficient H_2O_2 production.

To verify the important role of H^+ in –COOH at the initial stage, the dynamic changes of the surface potential on the catalysts were investigated by monitoring the zeta potential (Fig. 4i).[38] Under dark condition, no significant change is observed for the catalysts. After irradiation occurs, compared to BQ-TTB-COF and TTB-COF, the zeta potential of QL-TTB-COF exhibits a decreasing trend as O_2 is feed. This phenomenon is caused from the rapid deprotonation of –COOH, and the ionized H^+ acts as the "proton reservoir" and preferentially supplies H^+ to O_2 adsorbed at the dipyridyl N sites, thereby initiating the initial PCET process. As the irradiation time increases, its zeta potential distinctly rises, suggesting the H^+ on the surface is enriched by the WOR process. Subsequently, the H^+ is largely consumed in the ORR process, causing the zeta potential to decrease. As the photocatalysts are back to a dark environment, the zeta potential

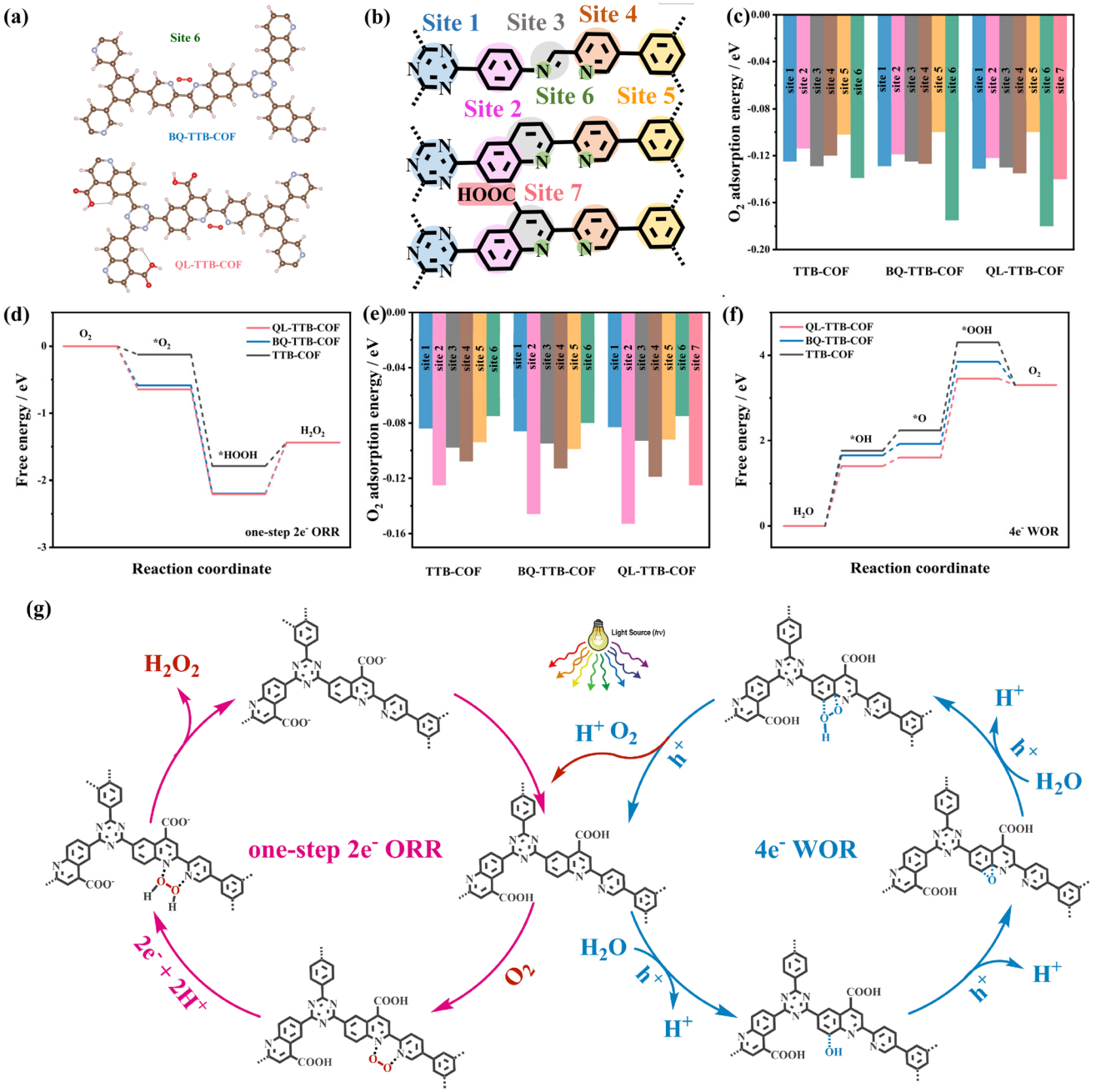

Fig. 5 (a) O_2 adsorption sites and configuration on the COFs, (b) potential O_2 adsorption sites of the COFs, (c) O_2 adsorption energy of the COFs, (d) diagrams of free energies of one-step $2e^-$ ORR, (e) H_2O adsorption energy of the COFs, (f) diagrams of free energies of $4e^-$ WOR, (g) possible reaction mechanism of the one-step $2e^-$ ORR and $4e^-$ WOR on QL-TTB-COF.

of QL-TTB-COF returns to be positive, demonstrating that the H^+ is accumulated. Additionally, the rate constant (K_f) for H_2O_2 generation was calculated during the first 12 min of the catalysis (Fig. S46), it is evident that the K_f of QL-TTB-COF (2.05 μmol g^{-1} h^{-1}) is significantly greater than BQ-TTB-COF (1.71 μmol g^{-1} h^{-1}) and TTB-COF (1.49 μmol g^{-1} h^{-1}). Noticeably, based on the independent gradient model derived from the Hirshfeld analysis, the dissociation enthalpy for proton release from –COOH and H_2O oxidation was determined (Fig. S47). It is clear that the dissociation enthalpy for proton release from –COOH (406 kJ mol^{-1}) is much less than that for H_2O oxidation (500 kJ mol^{-1}).[44] That is, at the initial stage for H_2O_2 production, the –COOH solves the problem of the delayed proton supply, supplying ample H^+ to accelerate the initial stage of the ORR by favorably initiating the PCET step. Subsequently, the ionized –COO^- anions take the function of the proton relays, facilitating the proton transfer in the pore channels to ensure the efficient activation and conversion of O_2.

The O_2 adsorption on the three COFs was thereafter carried out based on DFT calculations to understand the potential mechanism of the one-step $2e^-$ ORR and the $4e^-$ WOR process. The O_2 adsorption energies of the possible adsorption sites were initially calculated (Fig. 5a and S48–S53). As shown in Fig. 5b, the triazine ring, benzene ring (1), C=N bond, pyridine ring, benzene ring (2), and the imine N and pyridine N, as well as –COOH are set as Site 1, 2, 3, 4, 5, 6 and 7, respectively. Among the three COFs, Site 6 has the greatest O_2 adsorption energy and is therefore selected as the reference. Notably, QL-TTB-COF has the greatest adsorption energy (−0.18 eV) at Site 6 (Fig. 5c), significantly greater than BQ-TTB-COF (−0.17 eV) and TTB-COF (−0.13 eV). As shown in Fig. 5d, the formation of the *HOOH intermediate is the RDS in the one-step $2e^-$ ORR pathway. The corresponding energy barriers for TTB-COF, BQ-TTB-COF, and QL-TTB-COF are −2.83 eV, −1.61 eV and −1.59 eV, respectively. The lower energy barrier of QL-TTB-COF indicates that it more readily forms the intermediate *HOOH, thereby promoting H_2O_2 production.

For the $4e^-$ WOR process, the H_2O adsorption energies were calculated (Fig. 5e). It is obvious that Site 2 exhibits the greatest H_2O adsorption energy, with the values of −0.12 eV, −0.14 eV, and −0.15 eV for TTB-COF, BQ-TTB-COF, and QL-TTB-COF, respectively. In the $4e^-$ WOR pathway (Fig. 5f), the reaction from *O to *OOH is proven to be the RDS, with corresponding values of 2.06 eV, 1.93 eV, and 1.85 eV. These data confirm that QL-TTB-COF is more readily converted to O_2 *via* the $4e^-$ WOR pathway. Therefore, a possible photocatalytic mechanism is proposed in Fig. 5g. In the $2e^-$ ORR process, the photo-generated electrons in QL-TTB-COF rapidly migrate to the active dipyridyl N sites, which act as the thermodynamically favorable sites to capture and activate O_2. Benefiting from the localized proton environment established by the –COOH, the adsorbed O_2 undergoes a fast PCET process, it directly gains two e^- and two H^+ from the adjacent –COOH to form *HOOH intermediate, and further converts to H_2O_2. In the $4e^-$ WOR process, the photo-generated holes first oxidize H_2O to *OH at Site 2, which is then dehydrogenated to *O. Subsequently, another H_2O undergoes similar dissociation process, forming a new *OH. Ultimately, *O and *OH couple to produce O_2, and simultaneously release abundant H^+. Notably, the WOR process provides a continuous supply for the ORR. The released H^+ flows back by the hydrophilic channels to –COO^-, thereby forming –COOH. The produced O_2 is captured again by dipyridyl N, thus establishing a perfect closed-loop system. This dynamic synergy between O_2 adsorption and PCET process fundamentally ensures efficient and sustained operation of photocatalytic H_2O_2 production.

Conclusions

In summary, we developed a dual synergistic regulation strategy of COF photocatalysts targeting strong O_2 adsorption and rapid PCET process for H_2O_2 production. The synthesized COF photocatalyst, QL-TTB-COF, enables precise control of the photocatalytic microprocesses: at the thermodynamic level, the introduced highly stable quinoline rings reshape the local electronic structure at the active dipyridyl N sites, effectively overcoming the deficiency of insufficient electron affinity and hence enhancing Yeager-type side adsorption of O_2. At the kinetic level, the introduced –COOH improves the hydrophilicity of the pore channels, and more critically, it serves as the proton source in the initial ORR, which substantially lowers the energy barrier and establishes efficient proton transfer networks. Particularly, this ingenious regulation triggers the $4e^-$ WOR pathway. Through this synergistic "O_2 adsorption enhancement-proton pump acceleration" mechanism, QL-TTB-COF achieves an exceptionally high H_2O_2 yield rate of 7848 μmol g^{-1} h^{-1} (AQY = 8.8%). This work provides a novel paradigm to precise regulate the thermodynamic O_2 adsorption and the kinetic proton transfer process for efficient photocatalytic H_2O_2 production, and it also establishes a facile strategy for the rational construction of highly efficient COF photocatalysts.

Author contributions

Hao Wang: conceptualization, formal analysis, investigation, resources, data curation and writing. Junjiang Zong: methodology, formal analysis, investigation and resources. Shiyuan Wei: methodology and investigation. Meng Li: methodology and investigation. Lingfeng Zhu: methodology and investigation. Xiaodong Sun: methodology and investigation. Liqun Ye: methodology and investigation. Jianhan Huang: conceptualization, supervision, review & editing and project administration. Jiawei Li: conceptualization and supervision. You-Nian Liu: supervision and project administration. Tianyi Ma: supervision and project administration.

Conflicts of interest

There are no conflicts to declare.

Data availability

The data supporting this article have been included as part of the supplementary information (SI). Supplementary information is available. See DOI: https://doi.org/10.1039/d6sc01887d.

Acknowledgements

The National Natural Science Foundation of China (No. 22478442 and 22308389) and the 111 Project (D20015) were acknowledged for the financial supports.

Notes and references

1 B. Lin, D.-H. Si, J.-J. Li, S.-Y. Gao, X. Yang and R. Cao, *Adv. Mater.*, 2026, **38**, e20022.
2 J. Chen, S. Yan, F. Wang, F. Lin, J. Lin, R. A. Borse and Y. Wang, *Angew. Chem., Int. Ed.*, 2025, **64**, e202500924.
3 L. Li, X. Lv, Y. Xue, H. Shao, G. Zheng and Q. Han, *Angew. Chem., Int. Ed.*, 2024, **63**, e202320218.
4 H. Zhang, R. Ma, K. Chi, Y. Liu and Y. Zhao, *Angew. Chem., Int. Ed.*, 2025, **64**, e202516657.
5 A. Chakraborty, A. Alam, U. Pal, A. Sinha, S. Das, T. Saha-Dasgupta and P. Pachfule, *Nat. Commun.*, 2025, **16**, 503.
6 T. Xu, Z. Wang, W. Zhang, S. An, L. Wei, S. Guo, Y. Huang, S. Jiang, M. Zhu, Y.-B. Zhang and W.-H. Zhu, *J. Am. Chem. Soc.*, 2024, **146**, 20107–20115.
7 J. Cheng, Y. Wu, W. Zhang, L. Wang, X. Wu and H. Xu, *Adv. Mater.*, 2025, **37**, 2410247.
8 Z. Chen, H. Weng, C. Chu, D. Yao, Q. Li, C. Zhang and S. Mao, *Nat. Commun.*, 2025, **16**, 6943.
9 C. Sun, Y. Han, H. Guo, R. Zhao, Y. Liu, Z. Lin, Z. Xiao, Z. Sun, M. Luo and S. Guo, *Adv. Mater.*, 2025, **37**, 2502990.
10 T.-X. Luan, Q. Wei, C. Xin, S. Y. Wong, Y. Li, Y. Zheng, Y. Li, G. Liu, W. W. Yu, X. J. Loh, X. Li and P.-Z. Li, *Adv. Mater.*, 2026, **38**, e15517.
11 K. Yang, L. Chen, K. Xiong, J. Yang, M. Adeli, S. Li, M. Wang, C. Cheng and C. Zhao, *Adv. Funct. Mater.*, 2025, **36**, e20900.
12 G. Chakraborty, P. Das, B. Bhattacharya, C. Prinz, F. Emmerling and A. Thomas, *Chem. Sci.*, 2026, **17**, 4107–4115.
13 Y. Lin, J. Zou, X. Wu, S. Tong, Q. Niu, S. He, S. Luo and C. Yang, *Nano Lett.*, 2024, **24**, 6302–6311.
14 N. Mu, Z. Luo, W. Shan, H. Huang and H. Tang, *ACS Sustainable Chem. Eng.*, 2025, **13**, 16534–16543.
15 X. Ma, H. Pan, L. Gong, X. Ding, X. Zhou, H. Liu, R. Wang, C. Qu, Y. Zhao, D. Qi, Y. Bian and J. Jiang, *Angew. Chem., Int. Ed.*, 2025, **64**, e202511024.
16 D. Chen, W. Chen, Y. Wu, L. Wang, X. Wu, H. Xu and L. Chen, *Angew. Chem., Int. Ed.*, 2023, **62**, e202217479.
17 T.-X. Luan, Q. Wei, C. Xin, S. Y. Wong, Y. Li, Y. Zheng, Y. Li, G. Liu, W. W. Yu, X. J. Loh, X. Li and P.-Z. Li, *Adv. Mater.*, 2025, **38**, e15517.
18 C. Liu, X. Liu, B. Chen, Z. Li, X. Ou, Y. Lu, Y. Liu, C. Wu, S. Yao, Y. Liu, L. Ye, B. Han and Z. Yang, *Nat. Commun.*, 2025, **16**, 8941.
19 P. Huang, Y.-Y. Peng, X.-H. Wang, R.-H. Li, M.-H. Qin, M. Zhang, S.-M. Wang, M. Lu, S.-L. Li and Y.-Q. Lan, *Adv. Mater.*, 2026, **38**, e07849.
20 Z. Luo, X. Chen, W. Yang, Y. Chang, S. Zhu, F. Zhang, W. Lin, G. Xu, G.-E. Wang and X. Chen, *Sci. China Chem.*, 2025, **68**, 6639–6647.
21 D. Chen, W. Chen, G. Zhang, S. Li, W. Chen, G. Xing and L. Chen, *ACS Catal.*, 2022, **12**, 616–623.
22 W. Wu, Z. Li, S. Liu, D. Zhang, B. Cai, Y. Liang, M. Wu, Y. Liao and X. Zhao, *Angew. Chem., Int. Ed.*, 2024, **63**, e202404563.
23 K.-H. Xie, G.-B. Wang, F. Huang, F. Zhao, J.-L. Kan, Z.-Z. Chen, L. Cai, S.-L. Han, Y. Geng and Y.-B. Dong, *Nat. Commun.*, 2025, **16**, 3493.
24 P. Das, G. Chakraborty, J. Roeser, S. Vogl, J. Rabeah and A. Thomas, *J. Am. Chem. Soc.*, 2023, **145**, 2975–2984.
25 Y. Yang, L. Yu, T. Chu, H. Niu, J. Wang and Y. Cai, *Nat. Commun.*, 2022, **13**, 2615.
26 R. Wang, I. Nath, J. Chakraborty, L. Wang and P. Van Der Voort, *J. Mater. Chem. A*, 2025, **13**, 36375–36381.
27 Y. Zhang, Y. Liu, H. Li, G. Bai and X. Lan, *Chem. Eng. J.*, 2024, **489**, 151479.
28 N.-F. Wan, Y.-Q. Wang, L. Fu, J. Liu, B. A. Woodcock, Y.-Q. Hu, A. Eskelinen, A. Hector, M. Loreau, Y. Hautier, R. D. Bardgett, P. Kardol, D. Zuppinger-Dingley, L. H. Fraser, J. M. Bullock, S. Nakagawa, S. Shen, F. Xin, D.-P. Shi, Z. Li, J. Zhou and C. Scherber, *Nat. Ecol. Evol.*, 2026, **10**, 293–307.
29 Y. Ju, H. Lin, G. Tan, P. Su, Z. Wang, C. Hu, R. Hou, T. Hao, F. Chen and Y. Tang, *Nat. Commun.*, 2025, **16**, 5658.
30 C. Qin, X. Wu, L. Tang, X. Chen, M. Li, Y. Mou, B. Su, S. Wang, C. Feng, J. Liu, X. Yuan, Y. Zhao and H. Wang, *Nat. Commun.*, 2023, **14**, 5238.
31 Y. Luo, B. Zhang, C. Liu, D. Xia, X. Ou, Y. Cai, Y. Zhou, J. Jiang and B. Han, *Angew. Chem., Int. Ed.*, 2023, **62**, e202305355.
32 H. Wang, F. Zhou, S. Wei, M. Li, J. Li, J. Huang and Y.-N. Liu, *Appl. Catal., B*, 2026, **384**, 126234.
33 Q. Nan, J. Ning, B. Han, H. Wei, X. Wang, Y.-Y. Gu, S. Zhou, G. Cao, G. Zhang, X. Li, Y. Jia and L. Hao, *Chem. Sci.*, 2026, **17**, 466–474.
34 H. Xu, Y. Wang, Y. Xu, Q. Wang, M. Zhuang, Q. Liao and K. Xi, *Angew. Chem., Int. Ed.*, 2024, **63**, e202408802.
35 F. Hao, C. Yang, X. Lv, F. Chen, S. Wang, G. Zheng and Q. Han, *Angew. Chem., Int. Ed.*, 2023, **62**, e202315456.
36 T. Lu and S. Manzetti, *Struct. Chem.*, 2014, **25**, 1521–1533.
37 S. Manzetti and T. Lu, *J. Phys. Org. Chem.*, 2013, **26**, 473–483.
38 X. Sun, Y. Dong, T. Yang, Y. Ling, H. Zhao, J. Zhang and Y. Zhu, *Angew. Chem., Int. Ed.*, 2025, **65**, e24222.
39 Y. Chen, R. Liu, Y. Guo, G. Wu, T. C. Sum, S. W. Yang and D. Jiang, *Nat. Synth.*, 2024, **3**, 998–1010.
40 T. Lu and Q. Chen, *J. Comput. Chem.*, 2022, **43**, 539–555.
41 H. Cheng, Z. Ma, P. Kumar, H. Liang, Z. Cao, H. Xie, L. Cavallo, H. Kim, Q. Li, Y.-K. Sun and J. Ming, *Adv. Energy Mater.*, 2024, **14**, 2304321.
42 A. Yu, W. Liu, W. Xi, M. Mu and L. Shi, *Chem. Mater.*, 2024, **36**, 1880–1890.
43 H. Ooka, M. C. Figueiredo and M. T. M. Koper, *Langmuir*, 2017, **33**, 9307–9313.
44 H. Li, Y. Li, X. Lv, C. Liu, N. Zhang, J. Zang, P. Yue, Y. Gao, C. Liu and Y. Li, *Adv. Mater.*, 2025, **37**, 2415126.